be able to refine our previous results.
23. To make this estimate, we assume that only the phase-change boundary from γ spinel to perovskite is responsible for $S_{660}P$. We also assume that the shallowest $S_{660}P$ depth represents wave conversion in the ambient mantle. The temperature estimated for the coldest part of the Izu-Bonin slab is 900 ± 100 K (*41*), whereas the mantle temperature of the phase change from γ spinel to silicate-perovskite and magnesiowüstite near a depth of 660 km is 1900 ± 100 K (*6*).
24. E. Ito, M. Akaogi, L. Topor, A. Navrotsky, *Science* **249**, 1275 (1990).
25. R. van der Hilst, R. Engdahl, W. Spakman, G. Nolet, *Nature* **353**, 37 (1991).
26. Y. Fukao, M. Obayashi, H. Inoue, M. Nenbai, *J. Geophys. Res.* **97**, 4809 (1992).
27. Trench advance or trench retreat is relative to an immobile, or slowly moving, lower mantle.
28. R. D. van der Hilst and E. R. Engdahl, *Geophys. J. Int.* **106**, 169 (1991).
29. C. Park, K. Tamaki, K. Kobayashi, *Tectonophysics* **181**, 351 (1990).
30. T. Seno and S. Maruyama, *ibid.* **102**, 53 (1984).
31. Trench-advance rates over the last 5 million years increased linearly from 0 to 6 mm year^{-1} near Japan to 24 to 30 mm year^{-1} at a latitude of 27°N (*42*). Westward trench advance appears to have steepened the slab dip (*42*), which is roughly 50° near Japan and 80° near 27°N. The southern Izu-Bonin trench has only advanced toward Eurasia a maximum of 150 km in the last 5 million years, and the northern part has remained nearly fixed.
32. R. Jeanloz and E. Knittle, *Philos. Trans. R. Soc. London Ser. A* **328**, 377 (1989).
33. M. S. T. Bukowinski and G. H. Wolf, *J. Geophys. Res.* **95**, 12583 (1990).
34. L. Stixrude, R. J. Hemley, Y. Fei, H. K. Mao, *Science* **257**, 1099 (1992).
35. D. L. Anderson, *Theory of the Earth* (Blackwell, Boston, 1989).
36. J. Wahr, M. Ritzwoller, A. Rodgers, V. Dehant, *Eos* **73**, 518 (1992).
37. C. Sung and R. G. Burns, *Tectonophysics* **31**, 1 (1976).
38. S. H. Kirby, W. B. Durham, L. A. Stern, *Science* **252**, 216 (1991).
39. S. W. Roeker, *J. Geophys. Res.* **90**, 7771 (1985).
40. T. Iidaka and D. Suetsugu, *Nature* **356**, 593 (1992).
41. C. Meade and R. Jeanloz, *Science* **252**, 68 (1991).
42. R. L. Carlson and C. A. Mortera-Gutiérrez, *Tectonophysics* **181**, 331 (1990).
43. We use International Seismology Center (ISC) hypocenters that were determined from the direct *P* arrivals only. For some of the events the ISC catalog also contains hypocenters determined with *pP*, but for the sake of consistency, we use the hypocenters determined from *P*.
44. H. Jeffreys and K. E. Bullen, *Seismological Tables* (Smith and Ritchie, Edinburgh, 1970).
45. We thank E. R. Engdahl for access to his set of earthquake locations; R. Gritto and L. Stixrude for their helpful discussions; and J. Vidale, P. Shearer, and M. Bukowinski, whose comments helped improve the manuscript. Supported by National Science Foundation grant EAR9004026.

4 May 1993; accepted 29 July 1993

Comparisons Between Seismic Earth Structures and Mantle Flow Models Based on Radial Correlation Functions

Thomas H. Jordan, Peter Puster, Gary A. Glatzmaier, Paul J. Tackley

Three-dimensional numerical simulations were conducted of mantle convection in which flow through the transition zone is impeded by either a strong chemical change or an endothermic phase change. The temperature fields obtained from these models display a well-defined minimum in the vertical correlation length at or near the radius where the barrier is imposed, even when the fields were filtered to low angular and radial resolutions. However, evidence for such a feature is lacking in the shear-velocity models derived by seismic tomography. This comparison suggests that any stratification induced by phase or chemical changes across the mid-mantle transition zone has a relatively small effect on the large-scale circulation of mantle material.

One goal of structural seismology is to map variations in the seismic wave speeds in sufficient detail to resolve the pattern of the mantle convection. The most fundamental issue is the degree to which the large-scale flow is stratified by changes in mineralogical phase or bulk chemistry across the transition zone from depths of 400 to 700 km (*1*). Particular attention is being paid to the role of the 670-km discontinuity, which is dominated by the endothermic dissociation of spinel $(Mg,Fe)_2SiO_4$ into perovskite $(Mg,Fe)SiO_3$ plus (Mg,Fe)O. Laboratory (*2*) and seismic observations (*3*) constrain the Clapeyron slope of this phase transition to be negative and relatively steep: −4 ± 2 MPa K^{-1}. Convection calculations that combine phase-change dynamics with two-dimensional (2D) (*4, 5*) and 3D (*6, 7*) flow geometries indicate that an endothermic transition of this magnitude acts to inhibit convection through the phase boundary.

T. H. Jordan and P. Puster, Department of Earth, Atmospheric, and Planetary Sciences, Massachusetts Institute of Technology, Cambridge, MA 02139.
G. A. Glatzmaier, Earth and Environmental Science Division and Institute of Geophysics and Planetary Physics, Los Alamos National Laboratory, Los Alamos, NM 87545.
P. J. Tackley, Seismological Laboratory, California Institute of Technology, Pasadena, CA 91125.

Any restriction of the large-scale flow by this or some other mechanism (*8*) should be evident in the shear-wave speeds determined by seismic tomography. Seismic data sets have been inverted by several research groups (*9–13*) to obtain the shear-velocity perturbation $\delta\beta(r,\Omega)$ up to spherical harmonic degree 12 throughout the mantle, where r is the radius ranging from the core-mantle boundary at $b = 3480$ km to the surface at $a = 6371$ km and $\Omega = (\theta,\varphi)$, a point on the geographic sphere S_1. In regions where compositional and phase differences can be ignored, $\delta\beta(r,\Omega)$ is relatively small, typically less than 5% of the mean wave speed, and can be related to the aspherical temperature variations by the linear approximation

$$\delta\beta(r,\Omega) = (\partial\beta/\partial T)_P\, \delta T(r,\Omega) \qquad (1)$$

Progress in the calculation of 3D, solid-state convection (*6, 7, 14, 15*) makes it feasible to discriminate among the various stratification hypotheses by the comparison of numerical simulations of δT with seismic estimates of $\delta\beta$ throughout the entire mantle.

A direct comparison of the temperature and shear-velocity fields is not the best approach, however. Convection models are still too crude to predict the details of mantle flow. Moreover, whole-mantle (WM) tomography cannot resolve such details, and there is still considerable uncertainty in the value of $(\partial\beta/\partial T)_P$ in the lower mantle (*16*). Competing convection hypotheses must therefore be tested by consideration of the average properties of the temperature field that can be reliably derived from low-resolution estimates of the seismic velocities and that are robust with respect to the δT-$\delta\beta$ scaling. In most tomographic inversions, the shear-speed variations are represented by a truncated series

$$\delta\beta(r,\Omega) = \sum_{l=1}^{l_{\max}} \sum_{m=-l}^{l} \delta\beta_l^m(r) Y_l^m(\Omega) \qquad (2)$$

where $b \le r \le a$ and Y_l^m is the surface spherical harmonic of angular degree l and azimuthal order m. For hypotheses regarding convective stratification, the most obvious discriminants are radial functions constructed by some sort of averaging over the angular coordinates. An example is the angular squared-amplitude (power) spectrum, $S_\beta(r,l) = \sum_m |\delta\beta_l^m(r)|^2$. Tomographic estimates of $S_\beta(r,l)$ display high amplitudes and low characteristic wave numbers in both the uppermost and lowermost mantle (*9–12*). These estimates have been interpreted as manifestations of thermal, and perhaps chemical, boundary layers at the top and the bottom of the mantle (*9, 18*). The $S_\beta(r,l)$ spectrum peaks at l = 4 to 5 in the upper mantle (the scale of the tectonic plates) but has a strong $l = 2$ signature in the lower mantle, which some researchers have attributed to convective stratification (*19, 20*). On the other hand, a localized peak in total spectral variance expected for a stratification boundary (*5, 7, 21*) has not been observed in the vicinity of the 670-km discontinuity.

A better diagnostic of stratification is the radial correlation function

$$R_\beta(r,r') = \frac{1}{4\pi\sigma_\beta(r)\sigma_\beta(r')} \int_{S_1} \delta\beta(r,\Omega)\delta\beta(r',\Omega)d\Omega \quad (3)$$

where

$$\sigma_\beta^2(r) \equiv \frac{1}{4\pi} \int_{S_1} \delta\beta(r,\Omega)^2 d\Omega \quad (4)$$

This function is symmetric in the two radial coordinates and invariant with respect to any radial scaling of $\delta\beta(r,\Omega)$. It is unchanged by the root-mean-square (rms) normalization, for example, $R_\beta(r,r') = R_{\hat{\beta}}(r,r')$ for $\delta\hat{\beta}(r,\Omega) \equiv \delta\beta(r,\Omega)/\sigma_\beta(r)$. To the extent that $(\partial\beta/\partial T)_P$ depends only on pressure, Eq. 1 implies that $R_\beta(r,r') = R_T(r,r')$. Therefore, comparisons between the seismic and convection models on the basis of the radial correlation function are not sensitive to uncertainties in the temperature coefficient of shear velocity. The maximum value of the radial correlation function is unity, achieved on the diagonal $r = r'$, and its falloff away from this median ridge is indicative of the rate at which the structures on spherical surfaces decorrelate as their depths are separated. The vertical coherence in the vicinity of a radius r can be quantified by the radial correlation length $\rho_x(r)$, defined by the implicit equation

$$R_\beta(r - \rho_x/\sqrt{2},\ r + \rho_x/\sqrt{2}) = x \quad (5)$$

According to this definition, $\rho_x(r)$ is the half-width of the median ridge measured perpendicular to the diagonal out to some contour level $x < 1$. For $0.5 \lesssim x \lesssim 0.9$, the diagnostic properties of $\rho_x(r)$ are insensitive to the specific choice of x; we adopt a value of 0.75. Within a stratified system, $\rho_x(r)$ is expected to be maximized in regions where the vertical flux is high—for example, in the interior of convecting layers—and to be minimized at an internal boundary separating two layers.

For the convection simulations, we used 3D computer models (*14*) based on the anelastic and infinite Prandtl number approximations for thermal convection in a compressible, self-gravitating, spherical fluid shell (*22*). The models were run at total Rayleigh numbers of $\sim 2 \times 10^7$. In the WM simulation (Fig. 1), there were no changes in phase or chemistry with depth (*23*). The resulting flow is representative of 3D, WM models dominated by internal heating (*15*). The downwellings occurred primarily as narrow sheets, which broke up into cylinders as they descended, whereas the upwellings were generally weak and distributed, with a few concentrated plumes. The function $R_T(r,r')$ is characterized by a simple, ridge-like morphology, with relatively small variations near its diagonal. Away from the boundary layers, the half-width of the 0.75 contour, $\rho_{0.75}(r)$, ranges from a maximum of ~400 km in the upper mantle, where the downwelling sheets are best developed, to a minimum of ~200 km in the mid-mantle, where the cylindrical downwellings are most narrow (Fig. 2A, red lines). Other simulations demonstrate that the average of these two characteristic scales decreases as the Rayleigh number increases and that the ratio of the first to the second decreases as the ratio of internal heating to bottom heating is lowered (*24*). The flow in the WM model was highly time-dependent, but the basic structure of $R_T(r,r')$ in Fig. 1

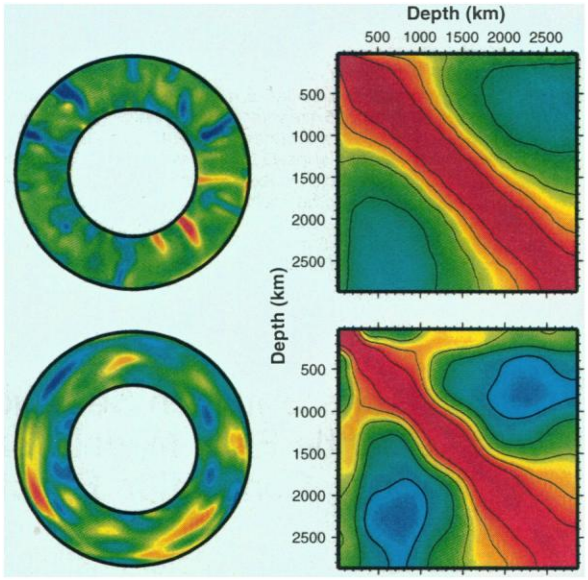

Fig. 1. (**Left**) Cross sections of aspherical, rms-normalized temperature fields $\delta\hat{T}_T$ and (**right**) plots of the radial correlation functions R_T for a snapshot of the whole-mantle (WM) convection simulation (*23*). (**Top**) The simulation at full resolution; (**bottom**) the same snapshot low-pass filtered to the nominal resolution of the seismic models (l_{max} = 10, n_{max} = 13). The colors on the cross sections vary from cold (blue) to warm (red) relative temperatures. The radial correlation is unity (red) along the diagonal; contours decrease in increments of 0.2 away from this axis of symmetry (cooler colors), with the thick contour denoting zero correlation. The convection calculations displayed in Figs. 1 and 3 were made with the use of the Intel Touchstone Delta System operated by the California Institute of Technology on behalf of the Concurrent Supercomputing Consortium.

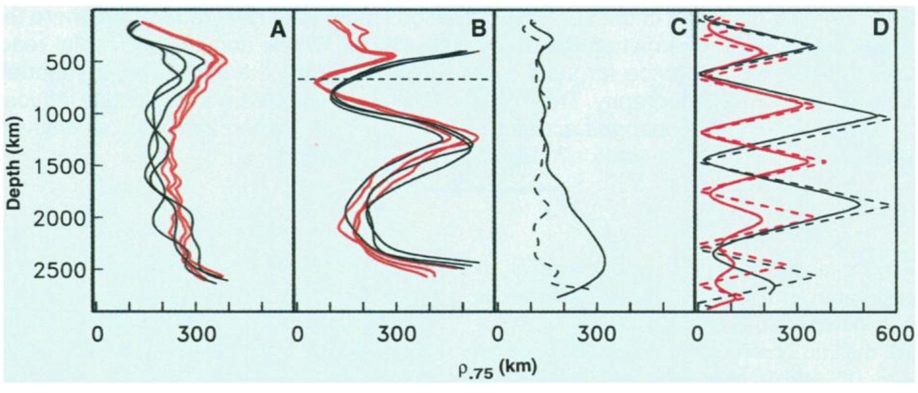

Fig. 2. Radial correlation length $\rho_{0.75}$ as a function of depth for (**A**) the unfiltered (red curves) and filtered (black curves) WM snapshots and (**B**) the unfiltered (red curves) and filtered (black curves) PC snapshots. One curve in each set corresponds to the snapshot in Figs. 1 or 3; we selected the other two to sample the temporal variability observed during the convection runs. (**C**) Radial correlation length for the two seismic models of Fig. 4: Harvard (solid curve) and Scripps (dashed curve). (**D**) Results of the Harvard resolving power experiments (*34*), showing $\rho_{0.75}$ for test structures specified by a single spherical-harmonic Chebyshev coefficient ${}_n\beta_l^m$. Dashed curves correspond to the input fields, and solid curves correspond to the fields recovered by inversion of the seismic data. The red curves are for the input harmonic $n = 8$, $l = 11$, and $m = 6$, and the black curves are for $n = 5$, $l = 10$, and $m = 5$. Although the resolving power calculations indicate that the tomographic inversions could detect a decorrelation at 670 km of the magnitude predicted by the PC simulation, such a feature is not observed in the seismic models.

persisted throughout the run (Fig. 2A).

Stratified flows show a different structure. The phase-change (PC) run of Fig. 3 included the dynamical effects of an endothermic phase transition at the 670-km discontinuity (*7*, *25*). In this simulation, downwellings in the upper mantle occurred in a network of interconnected sheets. Material pooled above the phase transition at the intersections of the sheets, breaking through into the lower mantle during brief episodes of high local mass flux (*7*). The avalanches from these flushing events formed large (~1000 km in diameter) cylindrical plumes, which sunk through the lower mantle and spread out in a thick layer at the core-mantle boundary (Fig. 3). Flow in the PC model is stratified in the sense that it has a local minimum in the normalized vertical mass flux at the phase boundary (*5*, *7*). The stratification is also evident as a distinctive pinch in the median ridge of $R_T(r,r')$ and as a corresponding minimum in the radial correlation length. The value of $\rho_{0.75}(r)$ at the phase boundary was 58 km, about one order of magnitude smaller than its mid-mantle maximum, and varied by only ±10% from snapshot to snapshot during the PC run (Fig. 2B). A more broad and shallow minimum in $\rho_{0.75}(r)$ occurred 700 to 800 km above the core-mantle boundary, delimiting a region in which colder material accumulates subadiabatically and diverges laterally at the base of the mantle.

The angular power spectra for the WM and PC models differ considerably (*26*), but in both cases the major features of the flow expressed in the radial correlation functions have low wave-number signatures. We low-pass filtered the models at angular degree and order 10 and radial order 13 to mimic the smearing that would occur if these structures were imaged by seismic tomography. Although this truncation obscured the details of the flow, including the thermal signature of all but the largest upwellings and downwellings, the morphology of $R_T(r,r')$ was largely unchanged. The filtering generally reduced the correlation lengths of the WM snapshots, suppressed their upper-mantle peaks, and increased their fluctuations (Fig. 2A, black lines). The graphs of $\rho_{0.75}(r)$ for the filtered PC snapshots lost some of the details associated with the surficial boundary layer, and the correlation-length minima corresponding to the phase change were increased to ~100 km and translated to slightly greater depths (Fig. 2B). However, the constriction of the median ridge at the phase change remained evident, as did the minimum defining the top of the accumulation zone in the lowermost mantle.

Radial correlation functions computed for other models of 3D convection in a spherical shell yielded similar results. Runs were done at lower Rayleigh numbers (~1.6 × 10^6) for WM models having different viscosity profiles, as well as for completely stratified models in which no mass flux was allowed across the 670-km discontinuity. The latter models approximated the stratification expected for a large, chemically induced density increase but did not include the boundary deformations expected in this situation (*27*, *28*). In the completely stratified models, $\rho_{0.75}(r)$ essentially goes to zero at the discontinuity; again, the minimum remains sharply defined when the snapshots are low-pass filtered [see (*28*) for correlation-function plots]. These models include simulations with a uniform viscosity profile, in which the coupling between the layers was primarily viscous, as well as runs with a 30-fold increase in viscosity in the lower mantle, where thermal coupling predominated. The addition of an exothermic olivine-spinel phase transition at a depth of 400 km to the PC model (*29*) reduced the characteristic time scale of material accumulation in the transition zone and so decreased the degree of stratification, but the deeper phase boundary was still marked by a well-defined minimum in $\rho_{0.75}(r)$.

For comparison, we computed the radial correlation function for two WM shear-velocity structures, the Harvard model SH12/WM13 and the Scripps model SH10C, which were derived from different data sets and parameterizations (*30*). The two maps of $R_\beta(r,r')$ are similar in the upper half of the mantle (Fig. 4), and the correlation lengths oscillate by only a few tens of kilometers about a mean of ~130 km (Fig. 2C). This value of $\rho_{0.75}$ corresponds to

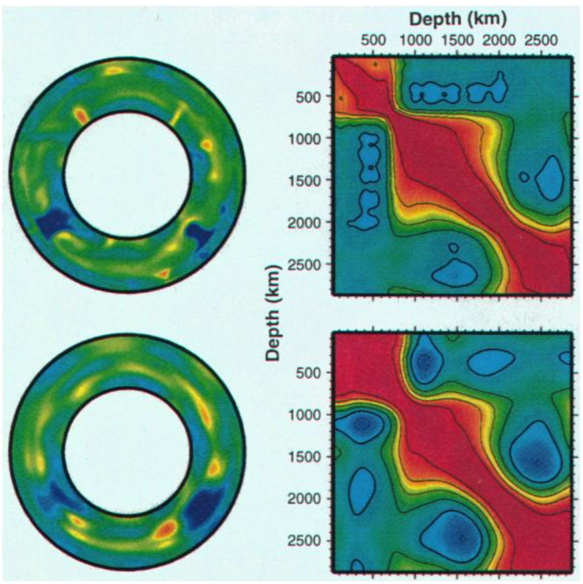

Fig. 3. (**Left**) Cross sections of aspherical, rms-normalized temperature fields $\delta\hat{T}$ and (**right**) plots of the radial correlation functions R_T for a snapshot of the phase-change (PC) convection simulation (*25*), which is partially stratified by an endothermic phase change at 670 km. (**Top**) The simulation at full resolution; (**bottom**) the same snapshot low-pass filtered to l_{max} = 10 and n_{max} = 13. The color scale and contour intervals are as in Fig. 1.

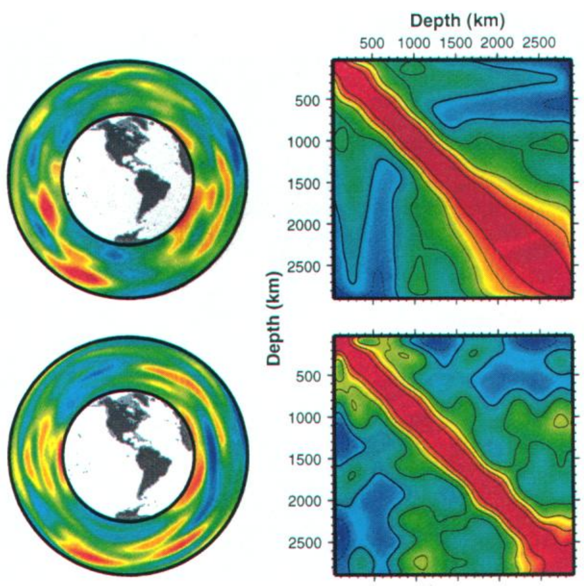

Fig. 4. (**Left**) Cross sections taken through the Greenwich meridian of the aspherical, rms-normalized shear-wave perturbations $\delta\hat{\beta}$ and (**right**) plots of the radial correlation functions R_β for two tomographic mantle structures: (**top**) the Harvard model SH12/WM13 and (**bottom**) the Scripps model SH10C. Both $\delta\hat{\beta}$ fields have been expanded to l_{max} = 10 and n_{max} = 13. On the cross sections, the colors vary from high- (blue) to low- (red) velocity anomalies. The radial correlation is unity (red) along the diagonal; contours decrease in increments of 0.2 away from the axis of symmetry (cooler colors), with the thick contour denoting zero correlation.

heterogeneity with a characteristic radial wave number of $n \approx 5$, consistent with the dominant vertical scale lengths observed in the cross sections of Fig. 4 (*33*). The inversions have good resolving power for features of this size throughout the upper and middle mantle (*34*), although there are significant discrepancies between the two seismic models in the lower mantle (*35*). The 670-km correlation-length minimum in the PC simulations is strongly expressed in these low wave numbers (truncation at $n_{\max} = 6$ decreases its amplitude by less than 50%). Therefore, if such a feature existed in the transition zone or upper part of the lower mantle, it would likely be recovered in inversions of the actual seismic data.

The most striking aspect of Figs. 2C and 4 is the lack of any discernible expression of the mantle transition zone. There is no evidence in either seismic model shown here, or in other published WM structures, for a decorrelation in shear-wave heterogeneity across the 670-km discontinuity (*36, 37*). The nearly constant value of $\rho_{0.75}(r)$ throughout the upper half of the mantle suggests that stratification of the magnitude observed in the PC simulation (*7*) or in the two-layer models (*28*) is not a present-day feature of the mantle's convective regime. This interpretation does not imply that the transition-zone phase changes are not dynamically significant or that chemical gradients in the vicinity of the 670-km discontinuity do not exist. It suggests only that their combined effects on the large-scale pattern of flow are sufficiently small to escape detection in the current generation of WM tomographic models.

Three-dimensional convection simulations do not yet account for the strong temperature dependence of viscosity. The inclusion of high-viscosity descending slabs may enhance the ability of cold downwellings to penetrate an endothermic phase change [for example (*27*)]. Therefore, one can envisage a regime in which weaker, smaller scale features of flow are dynamically inhibited at the 670-km discontinuity but also in which the average vertical mass flux through the transition zone, dominated by the plate-tectonic return flow, is not much less than those in the layers above and below it. Such a model would be consistent with the seismic data indicating the penetration of cold slab material into the lower mantle beneath zones in which the subduction flux has been historically large (*17, 38*) and would still provide an explanation for the observations of local distortions in slab geometry (*39*).

REFERENCES AND NOTES

1. The controversy was launched in nearly its present form at a symposium in Hershey, PA, in 1950, 15 years before the discovery of plate tectonics [F. Birch, *Trans. Am. Geophys. Union* **32**, 533 (1951); P. P. Bijlaard, *ibid.*, p. 535]. For more recent reviews, see T. H. Jordan, A. L. Lerner-Lam, K. C. Creager, in *Mantle Convection*, W. R. Peltier, Ed. (Gordon and Breach, New York, 1989), pp. 98–201; R. Jeanloz, *ibid.*, pp. 203–259; P. Olson, P. G. Silver, R. W. Carlson, *Nature* **344**, 209 (1990).
2. E. Ito, M. Akaogi, L. Topor, A. Navrotsky, *Science* **249**, 1275 (1990).
3. J. S. Revenaugh and T. H. Jordan, *J. Geophys. Res.* **96**, 19763 (1991).
4. P. Machetel and P. Weber, *Nature* **350**, 55 (1991); W. Zhao, D. A. Yuen, S. D. Honda, *Phys. Earth Planet. Inter.* **72**, 185 (1992); S. A. Weinstein, *Geophys. Res. Lett.* **20**, 101 (1993).
5. W. R. Peltier and L. P. Solheim, *Geophys. Res. Lett.* **19**, 321 (1992).
6. S. Honda, D. A. Yuen, S. Balachandar, D. Reuteler, *Science* **259**, 1308 (1993).
7. P. J. Tackley, D. J. Stevenson, G. A. Glatzmaier, G. Schubert, *Nature* **361**, 699 (1993).
8. Other mechanisms proposed for flow stratification include an increase in iron or silica content across the transition zone [F. M. Richter and C. E. Johnson, *J. Geophys. Res.* **79**, 1635 (1974); R. Jeanloz and E. Knittle, *Philos. Trans. R. Soc. London Ser. A* **328**, 417 (1989); L. Stixrude, R. J. Hemley, Y. Fei, H. K. Mao, *Science* **257**, 1099 (1992)] and an increase in viscosity [B. H. Hager and M. A. Richards, *Philos. Trans. R. Soc. London Ser. A* **328**, 309 (1989)].
9. T. Tanimoto, *Geophys. J. Int.* **100**, 327 (1990).
10. W.-J. Su and A. M. Dziewonski, *Nature* **352**, 121 (1991); A. M. Dziewonski and R. L. Woodward, *Acoust. Imaging* **19**, 785 (1991).
11. R. L. Woodward, A. M. Forte, W.-J. Su, A. M. Dziewonski, in "Evolution of the Earth and planets," *Geophys. Monogr. 79*, E. Takahashi, R. Jeanloz, D. Rubie, Eds. (American Geophysical Union, Washington, DC, 1993), pp. 89–109.
12. W.-J. Su, R. L. Woodward, A. M. Dziewonski, *Eos* **73**, 201 (1992); W.-J. Su, thesis, Harvard University (1992).
13. T. G. Masters, H. Bolton, P. Shearer, *Eos* **73**, 201 (1992).
14. G. A. Glatzmaier, *Geophys. Astrophys. Fluid Dyn.* **43**, 223 (1988).
15. J. R. Baumgardner, *J. Stat. Phys.* **39**, 501 (1985); G. Houseman, *Nature* **332**, 346 (1988); D. Bercovici, G. Schubert, G. A. Glatzmaier, *Science* **244**, 950 (1989); B. Travis, S. Weinstein, P. Olson, *Geophys. Res. Lett.* **17**, 243 (1990); G. A. Glatzmaier, G. Schubert, D. Bercovici, *Nature* **347**, 274 (1990); C. W. Gable, R. J. O'Connell, B. J. Travis, *J. Geophys. Res.* **96**, 8391 (1991).
16. Laboratory measurements [O. L. Anderson, D. Isaak, H. Oda, *Rev. Geophys.* **30**, 57 (1992)] and seismic observations of slab anomalies (*17*) yield reliable estimates of the temperature derivative of shear velocity at upper-mantle conditions, but there is considerable uncertainty in the value of $(\partial\beta/\partial T)_P$ in the lower mantle. The Debye-Grüneisen theory predicts that this value decreases substantially with pressure, perhaps by as much as an order of magnitude between the transition zone and the core-mantle boundary [T. S. Duffy and T. J. Ahrens, *J. Geophys. Res.* **97**, 4503 (1992)].
17. K. C. Creager and T. H. Jordan, *J. Geophys. Res.* **91**, 3573 (1986).
18. T. H. Jordan, *Proc. Natl. Acad. Sci. U.S.A.* **76**, 4192 (1979).
19. F. H. Busse, *Geophys. Res. Lett.* **10**, 285 (1983).
20. T. Tanimoto, *J. Phys. Earth* **38**, 493 (1990).
21. G. T. Jarvis and W. R. Peltier, *J. Geophys. Res.* **91**, 435 (1986).
22. The anelastic approximation allows for radial variations in the diffusivities and thermodynamic reference-state variables while filtering out acoustic waves, which propagate many orders of magnitude faster than the convective flow. The infinite Prandtl number approximation is justified by the large mantle viscosity. Each variable is expanded in a surface spherical-harmonic series truncated at angular degree and order $l_{\max}$ and a Chebyshev series truncated at radial order $n_{\max}$. A semi-implicit time-integration scheme numerically solves the fluid dynamic equations to determine the thermodynamic and convective velocity fields (*14*).
23. In the WM simulation (*7*), $l_{\max} = 127$ and $n_{\max} = 41$. The dynamic viscosity increased smoothly from 1.4×10^{22} Pa·s at the surface to 1.4×10^{23} Pa·s at the core-mantle boundary. The internal heating rate was 5.0×10^{-12} W kg^{-1}, and the superadiabatic temperature drop was 1000 K, yielding volume-averaged Rayleigh numbers of $Ra_I = 1.5 \times 10^7$ and $Ra_B = 5.5 \times 10^5$, respectively; the resulting basal heating fraction was 17%.
24. The dependence of $\rho_{0.75}(r)$ on Rayleigh number and internal heating fraction has been investigated by P. Puster, T. H. Jordan, and B. H. Hager [*Eos* **74**, 299 (1993)] using a 2D, cylindrically symmetric model that yields the same features in $R_T(r,r')$ as the 3D WM model. For example, these researchers found that the relative change in the depth-averaged value $\bar{\rho}_{.75}$ scales approximately as $-(1/3)\log Ra_B$.
25. The PC model (*7*) had the same angular resolution as did the WM model and a similar reference state, but separate Chebyshev expansions were used in the upper mantle ($n_{\max} = 17$) and lower mantle ($n_{\max} = 33$). The expansions were matched at the discontinuity with the use of a sheet-mass anomaly to represent the phase-change deflections, calculated for a Clapeyron slope of -4MPa K^{-1}. For numerical reasons, the zone of latent-heat release and absorption was spread over 25 km on either side of the boundary. The PC model was run at an internal heating rate of 2.75×10^{-12} W kg^{-1} ($Ra_I = 1.8 \times 10^7$) and a superadiabatic temperature drop of 1250 K ($Ra_B = 1.2 \times 10^6$); the resulting basal heating fraction was 40%.
26. The WM structures show a broad peak at high wave numbers ($8 \leq l \leq 20$), whereas the PC structures have their power concentrated at low wave numbers ($l \leq 7$) (*7*). The latter is in better agreement with the seismic data (*10*), although the significance of this observation is unclear because the convection models do not include rigid plates or floating continents, which modulate the flow pattern and redden its spectrum [M. Gurnis and S. Zhong, *Geophys. Res. Lett.* **18**, 581 (1991)].
27. U. R. Christensen and D. A. Yuen, *J. Geophys. Res.* **89**, 4389 (1984).
28. G. A. Glatzmaier and G. Schubert, *ibid.*, in press.
29. P. J. Tackley, D. J. Stevenson, G. A. Glatzmaier, G. Schubert, *Eos* **74**, 52 (1993).
30. The Harvard group (*12*) obtained spherical-harmonic Chebyshev coefficients for model SH12/WM13 ($l_{\max} = 12$, $n_{\max} = 13$) by inverting an extensive collection of long-period wave forms, including body and surface waves, as well as sets of *SS-S* and *ScS-S* differential travel times (*31*) and *S* and *SS* absolute travel times. The Scripps group derived model SH10C (*13*) using the same differential travel times in combination with their own absolute times of *S* phases and some higher order *S* multiples and a large compilation of free-oscillation data (*32*). They discretized the radial distribution of aspherical heterogeneity into 11 vertically homogeneous layers of varying thicknesses and expanded each in a spherical-harmonic series to $l_{\max} = 10$. For consistency, we truncated the coefficient series of the Harvard model at angular degree and order 10 and expanded the radial variation of the Scripps model in Chebyshev polynomials to order 13 (Fig. 3).
31. R. L. Woodward and T. G. Masters, *Nature* **352**, 231 (1991); *J. Geophys. Res.* **96**, 6351 (1991).
32. M. G. Ritzwoller, T. G. Masters, F. Gilbert, *J. Geophys. Res.* **93**, 6369 (1988); M. F. Smith and T. G. Masters, *ibid.* **94**, 1953 (1989).
33. The seismic value of $\rho_{0.75}$ above 1500 km is smaller than in the filtered WM simulation (compare Fig. 2, A and C). However, an increase in the Rayleigh number in the WM simulation to values more appropriate to the mantle ($Ra_I \approx 6 \times 10^7$, $Ra_B \approx 7 \times 10^6$) would probably correct the discrepancy (*24*).

34. In a series of experiments, the Harvard group inverted synthetic data sets calculated for shear-velocity structures specified by a single spherical-harmonic Chebyshev coefficient $_n\beta_l^m$. Figure 2D compares the radial correlation lengths computed from the input structures with the values for the recovered models for two examples, $_5\beta_{10}^5$ and $_8\beta_{11}^6$. In the first case, the inversion faithfully reproduces the $n = 5$ checkerboard pattern of $R_\beta(r,r')$ and the sawtooth variation of $\rho_{0.75}(r)$ to depths on the order of 2000 km. The second shows more degradation in the lowermost mantle as well as some loss of detail in the uppermost mantle, but even at these higher wave numbers ($n = 8$, $l = 11$) the correlation-length minimum near 670 km is reproduced with only a minor loss of amplitude.
35. The difference in the radial correlation functions for the two seismic models becomes large in the lowermost mantle (Fig. 2C), where the current data sets have poor resolving power (*34*). In the Harvard model, $\rho_{0.75}(r)$ begins to increase at a depth of 1500 km and reaches a maximum of 320 km at 2400 km, the depth that marks the best expression of the dominant high-amplitude, low-degree structures. In the Scripps model, these features are compressed into a thinner zone above the core-mantle boundary; $\rho_{0.75}$ remains approximately constant down to 2400 km, increasing to 270 km at the base of the mantle. These differing structures, which fit the data about the same, exemplify the nonuniqueness associated with the trade-off between radial and angular smoothness (G. Masters, personal communication, 1993).
36. Tanimoto (*20*) computed layer correlation coefficients for the degree-two components of his whole-mantle model MDLSH (*9*) and noted a low or negative correlation between layers above and below 1000-km depth, which he took as evidence for stratification. Individual spherical-harmonic components of whole-mantle convection simulations typically show strong, time-dependent radial decorrelations not evident in the heterogeneity fields expanded to $l_{max} \geq 6$. There is no evidence for a correlation-length minimum in Tanimoto's complete degree-six model.
37. We also examined two degree-eight tomographic models from an earlier Harvard study (*11*). The first, SH8/WM13, has the same radial parameterization as SH12/WM13 ($n = 13$), and its radial correlation function is similar to the one displayed in the top panel of Fig. 4. The second, SH8/U4L8, is parameterized by separate Chebyshev expansions in the upper mantle ($n = 4$) and lower mantle ($n = 8$) and therefore develops a discontinuity in $\delta\beta$ at a depth of 670 km. This model displays a sharp decrease in $\rho_{0.75}(r)$ confined to a 200-km interval centered on the 670-km discontinuity. This feature is much smaller in amplitude and radial scale than the decorrelation signatures associated with the stratified convection models discussed in the text and is probably an artifact of the discontinuous parameterization. A tomographic model can be represented as the output of a filter whose input is the real Earth and whose response is determined by the seismic data and the model parameterization. The transition-zone variation observed in the $\rho_{0.75}(r)$ values for SH8/U4L8 is reproduced almost exactly by the passing of an Earth structure having a smooth radial correlation function through the SH8/U4L8 parameterization filter. This calculation suggests that discontinuous model parameterizations should be avoided in tomographic tests of mantle stratification.
38. T. H. Jordan and W. S. Lynn, *J. Geophys. Res.* **79**, 2679 (1974); T. H. Jordan, *J. Geophys.* **43**, 473 (1977); S. P. Grand, *J. Geophys. Res.* **92**, 14065 (1987); K. M. Fischer, K. C. Creager, T. H. Jordan, *ibid.*, **96**, 14403 (1991).
39. D. Giardini and J. H. Woodhouse, *Nature* **307**, 505 (1984); K. M. Fischer and T. H. Jordan, *J. Geophys. Res.* **96**, 14429 (1991); R. van der Hilst, E. R. Engdahl, W. Spakman, G. Nolet, *Nature* **353**, 37 (1991); Y. Fukao, M. Obayashi, H. Inoue, M. Nenbai, *J. Geophys. Res.* **97**, 4809 (1992); P. M. Shearer and T. G. Masters, *Nature* **355**, 791 (1992).
40. We thank A. Dziewonski, W.-J. Su, and R. Woodward for their unpublished Earth models and resolution analysis; G. Masters, H. Bolton, and P. Shearer for their unpublished Earth model; and B. Hager for helpful discussions. Supported by grants from the U.S. National Science Foundation and by the Institute of Geophysics and Planetary Physics at Los Alamos National Laboratory.

6 May 1993; accepted 8 July 1993

Late Cretaceous Precessional Cycles in Double Time: A Warm-Earth Milankovitch Response

J. Park, S. L. D'Hondt, J. W. King, C. Gibson

Late Cretaceous climatic cycles are reflected in lithological and magnetic variations in carbonate sediments from South Atlantic Deep-Sea Drilling Project site 516F at a paleolatitude of roughly 30°S. Magnetic susceptibility cycles 20 to 60 centimeters in length appear to be controlled by the precession of the equinoxes. Cyclicity is particularly robust within a 24-meter interval in the lower Campanian, where overtone spectral peaks are observed as well as secondary susceptibility maxima within individual precession cycles. One model for this behavior is that sedimentation in the narrow Cretaceous South Atlantic was controlled by equatorial climate dynamics, with the precessional insolation signal rectified by the large land masses surrounding the ocean basin.

Quasi-periodic oscillations in the Earth's orbit about the sun cause variations in the amount and distribution of insolation received at the Earth's surface. In the last million years, the Milankovitch orbital cycles of precession, obliquity, and eccentricity are thought to have governed the Earth's climate (*1*). Orbital cycles exerted a strong influence on the climate of the Earth during the Cretaceous, as evidenced by cyclic variations in Cretaceous deep-sea and shelf sedimentary rocks (*2*). Because the fluctuations associated with orbital cycles are at most 10% of the mean insolation, the Earth's climate may often have been quite sensitive to externally determined conditions. As a consequence, the geologic record of orbital cycles shows how the Earth's climate responds to modest perturbations and may help us to anticipate future anthropogenic climate trends.

Mesozoic sedimentary records are often marred by large variations in accumulation rate and diagenesis (*3*). Fourier analysis of Mesozoic climate proxy data typically offers only a rough estimate of the data's spectral properties. Data of much higher quality can be found in drill cores from Deep-Sea Drilling Project (DSDP) site 516F, on the Rio Grande Rise in the South Atlantic Ocean. In one interval of these data, the accumulation rate appears nearly constant for roughly 1 million years, so that fine details of the climate proxy spectrum can be estimated. These details shed light on the climate dynamics of the warm Cretaceous.

The Cretaceous-Paleocene part of the site 516F data consists largely of alternating carbonate and marl layers of varying color, deposited at bathyal depths (500 to 1500 m) (*4*). In an earlier orbital-cycle analysis of this and other South Atlantic sites, optical densitometry was used to estimate an average duration of $23.5 \pm 4.4 \times 10^3$ years for the Cretaceous lithologic cycles (*5*), close to the principal modern precessional periods of 19.0×10^3, 22.4×10^3, and 23.7×10^3 years. We have measured whole-core magnetic susceptibility from core segments spanning the Santonian [~85 Ma (million years ago)] through the earliest Danian (~64 Ma). Magnetic susceptibility in carbonate sediments is influenced by many factors but is typically dominated by the ratio of terrigenous to biogenic components (*6*, *7*). Chalky layers typically have lower susceptibility than marly layers. Depending on the sedimentary environment, cyclic variations in susceptibility can be governed by terrigenous input, carbonate dissolution, or dilution by biogenic carbonate production.

Distinct cyclostratigraphic patterns appear to persist for a few tens of meters within the site 516F record, corresponding to intervals of a few million years. Cores 113, 114, and 115 are part of one such stable interval, lying within the lower Campanian (*8*) (Fig. 1). Short cycles are grouped into bundles of four or five, consistent with the modulation of precessional insolation variations by the Earth's orbital eccentricity. Drilling records (*4*) indicate that little material was lost between the core segments; core 115 is truncated, but the sum of cores 112, 113, and 114 differs by only 1 cm from nominal perfect

J. Park, Department of Geology and Geophysics, Post Office Box 6666, Yale University, New Haven, CT 06511.
S. L. D'Hondt, J. W. King, C. Gibson, Graduate School of Oceanography, University of Rhode Island, Narragansett, RI 02882.